

9-1-2023

Eta Carinae: The Dissipating Occulter Is an Extended Structure

Theodore R. Gull
NASA Goddard Space Flight Center

Henrik Hartman
Malmö Högskola

Mairan Teodoro
Space Telescope Science Institute

D. John Hillier
University of Pittsburgh

Michael F. Corcoran
NASA Goddard Space Flight Center

See next page for additional authors

Follow this and additional works at: https://scholarworks.sjsu.edu/faculty_rsca

Recommended Citation

Theodore R. Gull, Henrik Hartman, Mairan Teodoro, D. John Hillier, Michael F. Corcoran, Augusto Damineli, Kenji Hamaguchi, Thomas Madura, Anthony F.J. Moffat, Patrick Morris, Krister Nielsen, Noel D. Richardson, Ian R. Stevens, and Gerd Weigelt. "Eta Carinae: The Dissipating Occulter Is an Extended Structure" *Astrophysical Journal* (2023). <https://doi.org/10.3847/1538-4357/acdcf9>

This Article is brought to you for free and open access by SJSU ScholarWorks. It has been accepted for inclusion in Faculty Research, Scholarly, and Creative Activity by an authorized administrator of SJSU ScholarWorks. For more information, please contact scholarworks@sjsu.edu.

Authors

Theodore R. Gull, Henrik Hartman, Mairan Teodoro, D. John Hillier, Michael F. Corcoran, Augusto Damineli, Kenji Hamaguchi, Thomas Madura, Anthony F.J. Moffat, Patrick Morris, Krister Nielsen, Noel D. Richardson, Ian R. Stevens, and Gerd Weigelt



Eta Carinae: The Dissipating Occulter Is an Extended Structure

Theodore R. Gull^{1,2}, Henrik Hartman³, Mairan Teodoro², D. John Hillier⁴, Michael F. Corcoran^{5,6}, Augusto Daminieli⁷, Kenji Hamaguchi^{5,8}, Thomas Madura⁹, Anthony F. J. Moffat¹⁰, Patrick Morris¹¹, Krister Nielsen⁶, Noel D. Richardson¹², Ian R. Stevens¹³, and Gerd Weigelt¹⁴

¹ Exoplanets & Stellar Astrophysics Laboratory, NASA/Goddard Space Flight Center, Greenbelt, MD 20771, USA; tedgull@gmail.com

² Space Telescope Science Institute, 3700 San Martin Drive, Baltimore, MD 21218, USA

³ Materials Science & Applied Mathematics, Malmö University, SE-20506 Malmö, Sweden

⁴ Department of Physics & Astronomy & Pittsburgh Particle Physics, Astrophysics, & Cosmology Center (PITT PACC), University of Pittsburgh, 3941 O'Hara Street, Pittsburgh, PA 15260, USA

⁵ CRESST & X-ray Astrophysics Laboratory, NASA/Goddard Space Flight Center, Greenbelt, MD 20771, USA

⁶ The Catholic University of America, 620 Michigan Avenue, N.E. Washington, DC 20064, USA

⁷ Universidade de São Paulo, IAG, Cidade Universitária São Paulo-SP, Rua do Matão 1226, Butantã, São Paulo 05508-090, Brasil

⁸ Department of Physics, University of Maryland Baltimore County, 1000 Hilltop Circle, Baltimore, MD 21250, USA

⁹ Department of Physics & Astronomy, San Jose State University, One Washington Square, San Jose, CA 95192, USA

¹⁰ Dépt. de physique, Univ. de Montréal, C.P. 6128, Succ. C-V, Montréal, QC H3C 3J7, Canada

¹¹ California Institute of Technology, IPAC, M/C 100-22, Pasadena, CA 91125, USA

¹² Department of Physics & Astronomy, Embry-Riddle Aeronautical University, 3700 Willow Creek Road, Prescott, AZ 86301, USA

¹³ School of Physics & Astronomy, University of Birmingham, Birmingham B15 2TT, UK

¹⁴ Max Planck Institute for Radio Astronomy, Auf dem Hügel 69, D-53121 Bonn, Germany

Received 2023 April 18; revised 2023 June 6; accepted 2023 June 7; published 2023 August 25

Abstract

Previous Hubble Space Telescope (HST)/Space Telescope Imaging Spectrograph (STIS) longslit observations of Eta Carinae (η Car) identified numerous absorption features in both the stellar spectrum, and in the adjacent nebular spectra, along our line of sight (LOS). The absorption features became temporarily stronger when the ionizing far-ultraviolet radiation field was reduced by the periastron passage of the secondary star. Subsequently, dissipation of a dusty structure in our LOS has led to a long-term increase in the apparent brightness of η Car, an increase in the ionizing ultraviolet (UV) radiation, and the disappearance of absorption from multiple velocity-separated shells extending across the foreground Homunculus lobe. We use HST/STIS spectro-images, coupled with published infrared and radio observations, to locate this intervening dusty structure. The velocity and spatial information indicate the occulter is ≈ 1000 au in front of η Car. The Homunculus is a transient structure composed of dusty, partially ionized ejecta that eventually will disappear due to the relentless rain of ionizing radiation and wind from the current binary system along with dissipation and mixing with the interstellar medium. This evolving complex continues to provide an astrophysical laboratory that changes on human timescales.

Unified Astronomy Thesaurus concepts: [Massive stars \(732\)](#)

1. Introduction

Eta Carinae (η Car) caught the attention of southern observers in the early nineteenth century as its visual magnitude changed frequently (Smith & Frew 2011). By the 1840s its visual magnitude rivaled Sirius only to disappear to the naked eye, then marginally brightened in the 1890s and faded again. In the period 1939–1945 there was a jump by 1.2 mag in the visual brightness without brightening of the central star (Thackeray 1953). After that the brightening progressed at a slower pace (Gaviola 1950) to the present day when it has again achieved a visual magnitude ≈ 4.4 (Damineli et al. 2021).

The changing properties of η Car continue to fascinate astronomers. Since η Car is located relatively nearby (2300 pc; Smith 2006), ejecta are resolvable from η Car enabling studies not only of the central source, but the influence on material thrown out during historical times. Southern Hemisphere telescopes and space observatories with increasingly sophisticated instruments often turn to this amazing object to gain new

information as the spectra of the central source and its ejecta evolve. The apparent changes of η Car and its expanding ejecta make it an astrophysical laboratory that evolves on human timescales, enabling new studies of topics ranging from atomic and molecular physics to the evolution of massive stars nearing their end stages.

η Car ejected at least two shells of material within the historical record. Photographic imagery in the 1940s revealed a surrounding extended structure that Gaviola (1950) named the Homunculus. Near diffraction-limited imagery of the Hubble Space Telescope (HST) in the mid-1990s clarified the Homunculus to be a dusty, bipolar $10'' \times 20''$ structure with an equatorial skirt (Morse et al. 1998). Spectro-imagery from the HST/Space Telescope Imaging Spectrograph (STIS) identified an internal structure, the Little Homunculus, as a coaligned, ionized, bipolar $4'' \times 4''$ structure (Ishibashi et al. 2003). The Homunculus, by velocity and proper motion, is associated with the Great Eruption of the 1840s (Smith 2017) and the Little Homunculus is associated with the Lesser Eruption of the 1890s (Ishibashi et al. 2003).

η Car is a massive binary. The primary component is the closest example of a very massive star. Damineli (1996) and Damineli et al. (1997) used spectroscopic observations, correlated with the photometric near-infrared (NIR) light curve,



Original content from this work may be used under the terms of the [Creative Commons Attribution 4.0 licence](#). Any further distribution of this work must maintain attribution to the author(s) and the title of the work, journal citation and DOI.

to discover the 5.5 yr binary cycle of η Car. Corcoran (2005) confirmed the binary period in X-rays using the Rossi X-ray Timing Explorer (RXTE). RXTE spectra analyzed by Ishibashi et al. (1999) showed that the wind velocity of the companion star was at least a factor of 3 higher than the wind velocity of the primary star, while comparison of Chandra X-ray grating spectra with wind–wind collision models by Pittard & Corcoran (2002) provided mass-loss rate estimates, $\dot{M}_A \approx 2.5 \times 10^{-4} M_\odot \text{ yr}^{-1}$ and $\dot{M}_B \approx 10^{-5} M_\odot \text{ yr}^{-1}$ with $V_{\infty,A} \sim 500$ to 700 km s^{-1} and $V_{\infty,B} \sim 3000 \text{ km s}^{-1}$.

More recent refinements are the binary period, $P = 5.53 \text{ yr}$ (Teodoro et al. 2016) with the primary mass $\gtrsim 100 M_\odot$ (Hillier et al. 2001, 2006), $\dot{M}_A = 8.5 \times 10^{-4} M_\odot \text{ yr}^{-1}$ (Madura et al. 2013) and $V_{\infty,A} = 420 \text{ km s}^{-1}$ (Groh et al. 2012b). The secondary, η Car-B, is estimated to have a mass ≈ 30 to $50 M_\odot$ (Verner et al. 2005; Mehner et al. 2010). The secondary properties remain inferred as direct measure of the secondary is yet to be accomplished because of the huge contrast in brightness between the companions. A possible exception may be the recent study by Strawn et al. (2023) that tracked the weak He II $\lambda 4686$ emission to measure the radial velocity orbit of the secondary directly, which moves in antiphase relative to the primary star; they find a minimum mass of $55 M_\odot$ for η Car-B with a minimum mass for η Car-A of $102 M_\odot$.

The observed optical and ultraviolet (UV) flux of η Car, monitored by multiple facilities from the ground and in space, has increased over the past two decades. The response of the dusty Homunculus, serving as a calorimeter to the $6 \times 10^6 L_\odot$ source, has been constant for nearly a half century other than a possible modulation due to the binary orbit (Mehner et al. 2019). The X-ray light curve also has been repeatable (Corcoran et al. 2010; Espinoza Galeas 2021). Damineli et al. (2019) noted that while the flux of η Car at visible wavelengths increased by an order of magnitude, the contribution of scattered starlight from the Homunculus stayed constant, demonstrating that the recent changes in η Car were apparently due to a dusty occulter that has been dissipating and/or moving out of the line of sight (LOS).

Hillier & Allen (1992), Hillier et al. (2001), and Hillier et al. (2006) previously noted that the equivalent width of H α measured directly for η Car was inconsistent with atmospheric models by CMFGEN and was larger than measured in the scattered starlight off the Homunculus. They suggested that an occulting structure, with very gray spectral properties, systematically blocked the source of the stellar continuum more than the very extended wind of η Car-A.

Furthermore, Weigelt et al. (1995) suggested the existence of an occulting structure in front of η Car to explain the unusually high relative brightness of three ejected clumps at separations of $0''.1$ to $0''.3$ (Weigelt & Ebersberger 1986). These three clumps were only 1.3–2.4 mag fainter than the central star η Car in the wavelength region of 8000–9000 Å in 1983 when they were discovered and only a factor of two fainter than η Car in the UV at 2000 Å in 1991 and 1992 (Davidson et al. 1995).

The long-term decrease of the emission lines and the increase in optical depth of P Cygni absorption were replicated by a model simulating a dissipating occulter in front of a stable primary star (Damineli et al. 2022). Damineli et al. (2021) predicted that by the 2030s, the occulter will have completely dissipated. Recently Pickett et al. (2022) showed that the long-term evolution of the Na D absorption from the Little Homunculus was consistent with a disappearing occulter.

The tenfold increase in far-ultraviolet (FUV)¹⁵ (Gull et al. 2021, 2022) since 2000 has affected many of the three dozen shells ranging in velocity from -121 to -1074 km s^{-1} in the LOS as cataloged in the near-ultraviolet (NUV) by Gull et al. (2006). K. Nielsen et al. (2023, in preparation) found that nearly all of the ~ 800 strong absorption lines of H $_2$ (-513 km s^{-1} , associated with the Homunculus) disappeared and most of the low-ionization signatures of absorption systems between -122 and -186 km s^{-1} , associated with the Little Homunculus, likewise disappeared. Current evidence suggests that slower-moving shells, being closer to η Car, are now more highly ionized and that the H $_2$ has been destroyed by the increased extreme-ultraviolet (EUV) and FUV radiation escaping from the central region.

In this discussion we examine archived spatially resolved NUV HST/STIS spectra (spectro-images)¹⁶ that include portions of the foreground ejecta to estimate the spatial extent of the dissipating occulter. Section 2 reviews the geometry of the Homunculus and Little Homunculus. Section 3 catalogs the selected spectro-images that provide temporal information on the dissipating occulter. Section 4 describes the spatially resolved, high-velocity nebular structures that respond to the high- and low-ionization states of the 5.5 year binary period and which exhibited long-term changes. Section 5 provides insight on where the occulter/absorber is located. A brief conclusion is in Section 6.

2. Setting the Stage

We view the bipolar Homunculus with its axis of symmetry projecting at $\approx 45^\circ$ to the sky plane and tilted on the sky with the foreground lobe in the southeast. η Car is physically centered between the two lobes with its orbital plane perpendicular to the Homunculus axis of symmetry (Madura et al. 2012). From our vantage, the stellar position projects, as shown in Figure 1, close to an edge of the foreground lobe, leading to a noticeable velocity shift across the nebular structure as shown below. Immediately surrounding η Car is a complex of dusty ejecta that strongly scatters starlight out to $1''$ diameter (2300 au). Clumps of emission are scattered throughout this complex, the brightest of which are Weigelt C and D, two clumps first noticed by NIR speckle interferometry to be nearly as bright as η Car itself (Weigelt & Ebersberger 1986). Proper motion studies, most recently done by Weigelt & Kraus (2012), indicate these clumps were ejected in the Lesser Eruption. Davidson et al. (1995), using data from the HST/Faint Object Spectrograph (FOS), determined these to be emission-line structures photoionized by η Car. Detailed mapping of the emission clumps in [Fe II] and [Fe III] and the variation in ionization across one orbital period were described by Gull et al. (2016).

The long, thin rectangle superimposed on Figure 1, defines the position of a $3''.2$ long segment of the HST/STIS $52'' \times 0''.1$ aperture oriented at position angle (PA) = 332° , marking the portion of the Homunculus sampled in the spectro-images displayed in Figures 3, 4, A1, and A2. The aperture extends

¹⁵ Following the HST/STIS echelle spectral modes, we define NUV to be 1750–3150 Å (E230H and E230M), FUV to be 1215–1750 Å (E140H and E140M) and the EUV to be shortward of 1216 Å (Ly α).

¹⁶ Based on archived observations made with the NASA/ESA HST, obtained at the Space Telescope Science Institute, which is operated by the Association of Universities for Research in Astronomy, Inc., under NASA contract NAS5-26555.

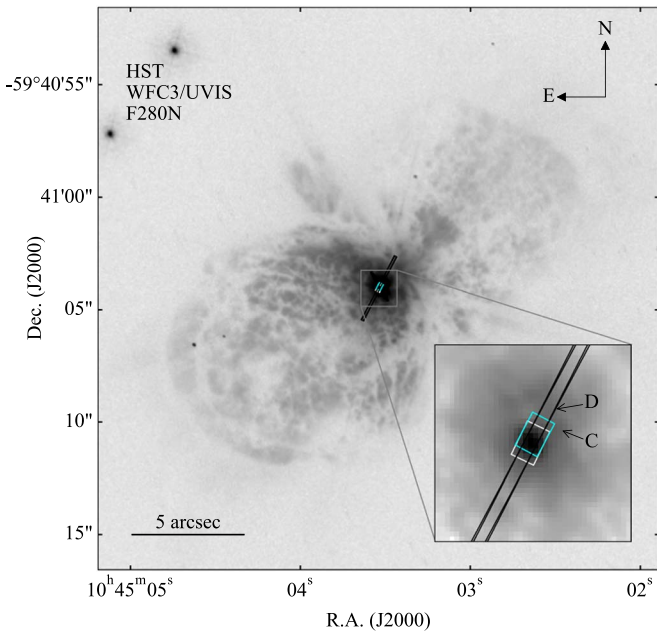


Figure 1. HST image of the Homunculus and the central source recorded with the WFC3/UVIS instrument and the F280N filter on 2020 February 12 ($\Phi = 13.997$). The $3.2'' \times 0.1''$ long portion of the $52'' \times 0.1''$ aperture is indicated by the long, black rectangle (used for the spectro-images displayed in Figures 3, 4, 5, A.1, and A.2). The shorter white and cyan rectangles (see enlargement) indicate the positions of the $0.3'' \times 0.2''$ aperture used with the HST/STIS echelle spectrograph for the spectro-images displayed in Figure 5, top and bottom. The positions of Weigelt C and D are indicated in the $1.6'' \times 1.6''$ inset image. The projected edge of the foreground lobe is located $\approx 1.3''$ NNW of η Car. (Image is from the HST archive.)

from south by southeast (SSE) across the position of η Car to north by northwest (NNW) ending at the apparent edge of the foreground lobe of the Homunculus. This aperture position had been selected to monitor changes in Weigelt B and D, located $0.2''$ and $0.3''$, respectively, to the north by northeast (NNE) of η Car, as their ionization changed between the high-ionization and low-ionization states by direct radiation from η Car-B. The Weigelt B clump is no longer detected.

The white rectangle in the enlargement within Figure 1 outlines the position of the $0.2'' \times 0.3''$ aperture centered on η Car for the HST/STIS echelle spectro-image recorded at $\phi = 11.037$, a portion of which is displayed in Figure 5, top. The cyan rectangle shows the position of the spectro-image recorded at $\phi = 11.119$ (Figure 5, bottom), offset $0.1''$ NNW from η Car, which placed the star at the edge of the aperture and allowed sampling the changes in front of Weigelt B and D during the early recovery to the high-ionization state.

A sketch, displayed in Figure 2, relates the locations in the LOS from η Car of the two major shell complexes, the Homunculus (-513 km s^{-1}), and the Little Homunculus (-146 km s^{-1}). Gull et al. (2006) found many fainter velocity components in absorption lines of singly ionized metals clustering around these two strongly defined velocities in the NUV (HST/STIS E230H spectra) recorded between 2000 and 2004. The dissipating occulter, of unknown geometry sketched as a gray rectangle, led to weakening or disappearance of the absorption at all velocities. In the FUV spectra (HST/STIS G230MB) recorded from 2018 to 2019, the weakened -513 km s^{-1} and very weak -146 km s^{-1} velocity components remain.

3. Observations

This study was motivated by the desire to understand what was changing within the Homunculus, given the noticeable increase in flux in the FUV (Gull et al. 2020) and whether the archived spectra could provide the structure and location of the occulter. Multiple spectra had been recorded of η Car and the Homunculus by various programs with the HST/STIS beginning in early 1998 extending through 2021. We examined each of the spatially resolved spectra looking for evidence of absorption signatures from the multiple shells cataloged in the LOS by Gull et al. (2006) and changes thereof with time. Of the hundreds of HST/STIS spectra recorded of η Car, we list in Table 1 the spectro-images that showed the most informative spatial and/or velocity changes in absorption from the high- to low-ionization states and/or across the long term, nearly two decades of time. Spectro-images at the same PA, or its 180° compliment, were required.

The scattered starlight drops by an order of magnitude within a few arcseconds of η Car. While in early observations the full spectral range of the CCD was sampled from 1713 \AA – 10000 \AA , the useful spectral absorption signatures of the intervening shells proved to be from singly ionized metal lines in the 2500 to 2800 \AA spectral interval. The strongest, best defined absorptions originated from resonant or near-resonant energy levels.

The STIS $52'' \times 0.1''$ aperture sampled the extended structure centered on η Car, whose characteristics change rapidly with PA. Fortunately a series of observations was systematically centered on η Car at PAs near 332° or its complement, $+152^\circ$, during the extended high-ionization state and the transient low-ionization state associated with the binary periastron passage. The CCD pixels were sampled at $0.05''$ intervals, which were an adequate match with the $0.1''$ width of the aperture. The nominal spectral resolving power was $R = \lambda/\delta\lambda = 8000$. Spectro-images recorded along the central portions of the aperture are presented in Figures 3, 4, A1, and A2.

Higher spectral and spatial resolutions were obtained with the STIS echelle modes at resolving power $R = 110,000$, using a $0.3'' \times 0.2''$ aperture (the reductions of which are not supported by STScI), in combination with the E230H grating mode. The NUV Multi Anode Multi Array (MAMA) echelle data were processed by STIS science team software at a spatial resolution of $0.075''$ sampled at intervals of $0.0125''$ along the projected width of the aperture, resulting in the spatially resolved imagery displayed in Figure 5. Line-by-line spectral extractions were accomplished using STIS science team tools which enabled spatially resolved spectra of specific structures as imaged through the aperture.

4. Absorption Changes Within the Homunculus and the Little Homunculus

In this section, we highlight changes in the high-velocity absorptions ($>100 \text{ km s}^{-1}$) that occur within the the spatially extended Homunculus foreground lobe due to FUV-induced ionization. Section 4.1 describes changes brought on by the transient decrease of FUV radiation from the high-ionization state across cycle 10 to the low-ionization state at the beginning of cycle 11 when the FUV radiation from the secondary star is briefly absorbed by the extended primary wind. In Section 4.2, we describe the strong decrease and velocity narrowing of absorptions between the high-ionization states of cycles 10 and

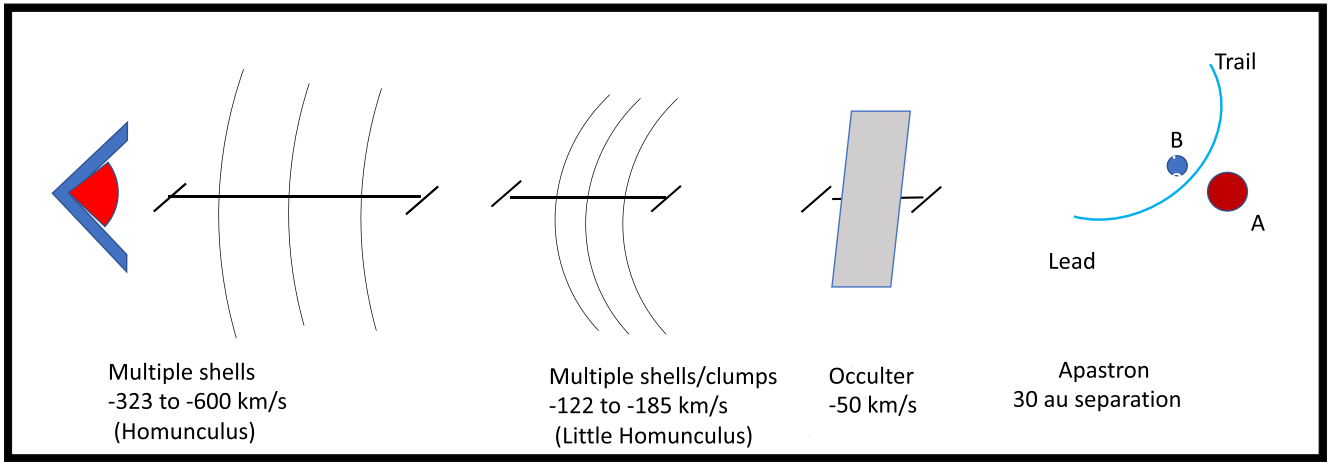


Figure 2. Sketch of the structures within the Homunculus as seen along our LOS (not to scale). Is the occulter a portion of the Little Homunculus or a dense clump, like the Weigelt clumps that appear to be within several hundred astronomical units of the binary? In the NUV spectra recorded between 2000 and 2004, multiple, weaker shells at various velocities clustered near -513 km s^{-1} , associated with the Homunculus and the 1840s Great Eruption, were identified (Gull et al. 2006). Additional shells clustered in velocities above and below -146 km s^{-1} are associated with the Little Homunculus ejected in the 1890s Lesser Eruption. By 2018, signatures of most of the weaker shells had disappeared. For scale, the strongest component of the Homunculus, moving at -513 km s^{-1} since the 1840s, is about $1.8 \times 10^4 \text{ au}$ and the Little Homunculus, moving at -146 km s^{-1} since the 1890s, is about $3 \times 10^3 \text{ au}$ in front of $\eta \text{ Car}$. The occulter and the interacting winds are associable with or within the Little Homunculus (see Figure 9). The reader may note that the shape and extent of the occulter remains uncertain.

Table 1
Log of the HST/STIS Observations Used in This Study

Date	HST Program	ϕ^a	Aperture	Grating	PA ^b	Central Wavelength
2000-03-20	8327	10.404	$52'' \times 0''1$	G230MB	+332°	2557 Å, 2697 Å
2003-09-21	8327	11.037	$0''3 \times 0''2$	E230H	+154°	2762 Å
2003-09-22	9973	11.037	$52'' \times 0''1$	G230MB	+153°	2557 Å
2004-03-06	9973	11.119	$0''2 \times 0''2$	E230H	+333°	2762 Å
2018-04-21	15067	13.641	$52 \times 0''1$	G230MB	+333°	2557 Å, 2697 Å
2019-06-10	15611	13.886	$0''2 \times 0''2$	E140H	+82°	1234 Å, 1416 Å, 1598 Å

Notes.

^a ϕ refers to the binary orbital phase plus spectroscopic cycle based upon both the disappearance of He II emission and the X-ray drop with periastron passage numbered 13 occurring on JD 2456874.4 \pm 1.3 days and with an orbital period of 2022.7 \pm 0.3 days (Teodoro et al. 2016). While in general agreement with the period, the observations and models do not concur on the actual periastron event, which is thought to be several days earlier than this reference date. The periastron number refers to the convention established by Groh & Daminieli (2004) based upon spectroscopically detected periastron beginning in 1948 February.

^b The PA of the aperture. Note that some observations were recorded at or near the complementary PA = 152°. Where necessary the spectro-image was mirror-imaged in the figures to match the spatial position.

13 triggered by the long-term tenfold increase in FUV radiation. Much stronger absorption complexes exist in the 2000–2200 Å spectral region but saturation, along with increased crowding of absorption lines, provided limited information on the spatial variations with time.

In the following two subsections, we discuss the multiple changes using two isolated metal absorption lines (Table 2).

1. The Mn II $\lambda 2577$ line, which originates from the ground state (0 eV), is representative of resonant metal lines found in or near the spectral interval from 2570 to 2610 Å (see Figure A1 and Table A1).
2. The Fe II $\lambda 2757$ line, which originates from an energy level 1.0 eV above the ground state, is representative of metal lines found in or near the spectral interval from 2730 to 2760 Å (see Figure A2 and Table A1).

The behaviors of the resonant and near-resonant absorption lines, while similar, are sufficiently different to reveal changes in ionization and excitation in the multiple velocity-defined shells originally cataloged by Gull et al. (2006). Of the 36 velocity-defined shells identified in the LOS, most velocities

clustered around -146 and -513 km s^{-1} with velocity separations averaging 12–15 km s^{-1} . The velocity resolution of the longslit spectra using STIS G230MB is about 40 km s^{-1} in this spectral interval, which is insufficient to resolve individual velocity components. Only the echelle spectro-images, which provided 3 km s^{-1} resolution in the LOS from $\eta \text{ Car}$, separated the individual components (see Section 4.3). The CCD spectro-images only prove that the multiple, faint velocity components are present or absent.

4.1. Absorption Changes from the High- to Low-ionization States

Absorption by singly ionized metals increases from the high- to low-ionization states due to a drop in EUV and FUV radiation when the EUV-dominating secondary briefly plunges into the extended primary wind. The NUV spectro-images, as displayed in Figure 3, qualitatively show an increase in nebular absorption from $\phi = 10.404$, deep in the high-ionization state, to $\phi = 11.037$, deep in the low-ionization state.

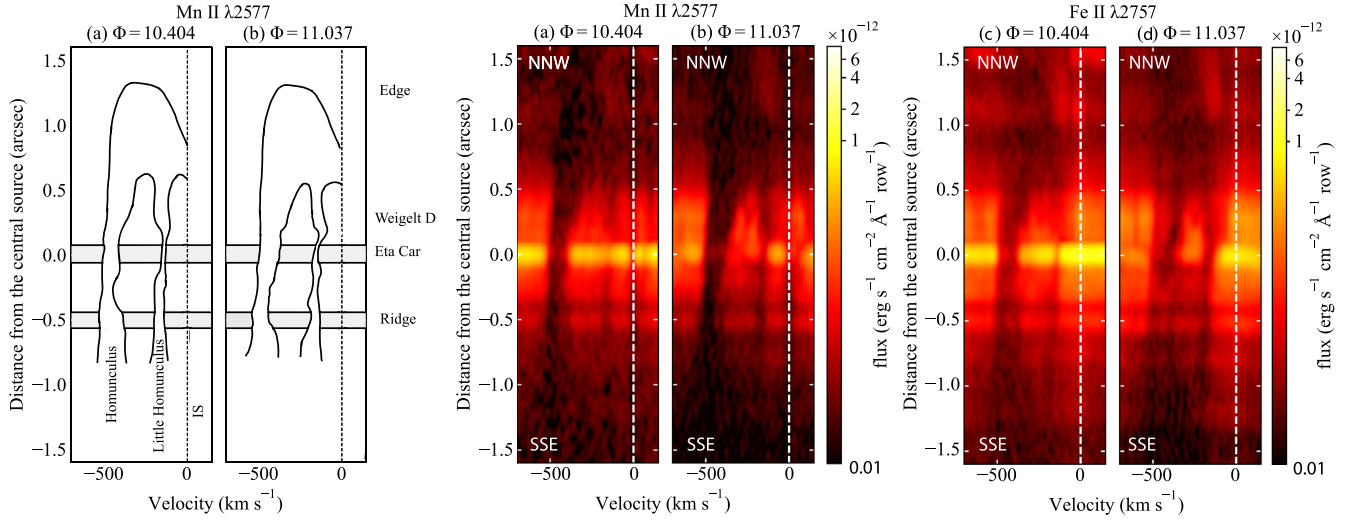


Figure 3. Phase-dependent changes from the high- to low-ionization states of spatially varying absorption by foreground ejecta. Left: sketch of the absorption structures between the two states. Velocities are referenced to the ISM (≈ 0 km s⁻¹). Middle: changes occurring in the Mn II $\lambda 2577$ line, which originates from the ground state, 0.0 eV, in the short term between (a) the high-ionization state at $\phi = 10.404$ and (b) the low-ionization state at $\phi = 11.037$. Right: changes occurring in the Fe II $\lambda 2757$ line, which originates from a level 1.0 eV above the ground state for (c) $\phi = 10.404$ and (d) $\phi = 11.037$. The dashed line in each spectro-image represents 0 km s⁻¹. The sketch includes labeling of the projected Homunculus edge, located $\approx 1''.3$ NNW of η Car and the ridge of backscattered starlight which is discussed in Section 5.2. The spectro-images at $\phi = 11.037$, recorded at PA = 152°, are mirror-imaged in this figure for comparison with the spectro-images at $\phi = 10.404$, recorded at PA = 332°.

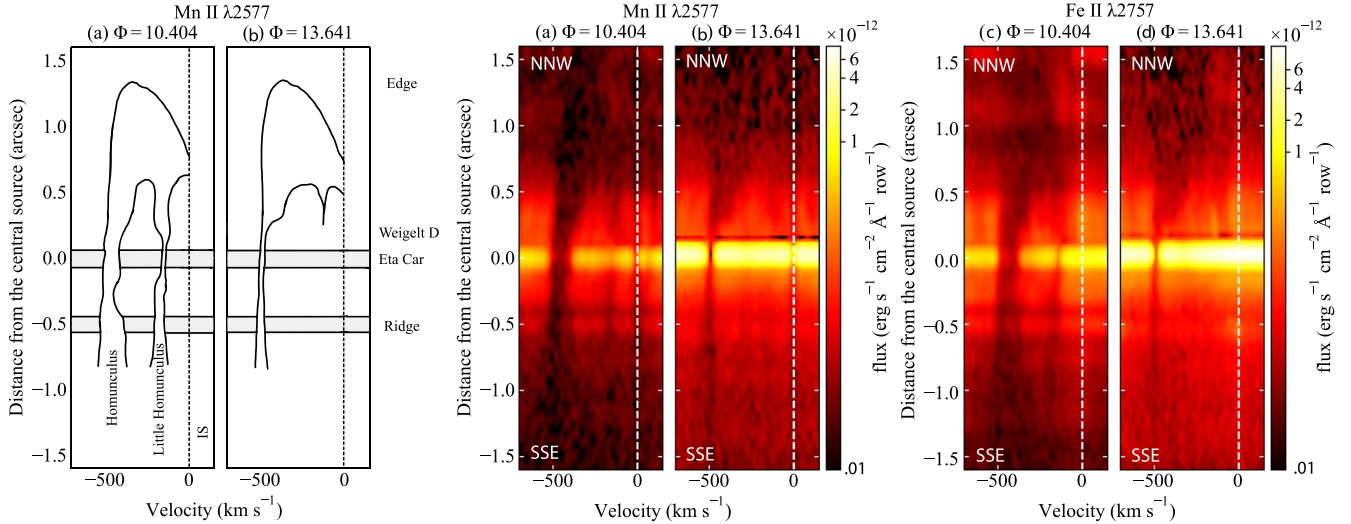


Figure 4. Long-term, ~ 18 yr interval, changes of spatially varying absorption by foreground ejecta between the high-ionization states of cycles 10 and 13. Left: sketch of the absorption structures and how they change over the long term. Middle: strong changes occur in the resonant Mn II $\lambda 2577$ line between (a) the high-ionization state at $\phi = 10.404$ and (b) the high-ionization state at $\phi = 13.641$. Right: similar changes occur in the Fe II $\lambda 2757$ line, which originates above the ground state (1 eV) for (c) $\phi = 10.404$ and (d) $\phi = 13.641$. The dashed line represents 0 km s⁻¹, which is present from an interstellar cloud in Mn II but not in Fe II. The sketch includes labeling of the projected Homunculus edge, located $\approx 1''.3$ NNW of η Car and the ridge of backscattered starlight, which is discussed in Section 5.2. Broad absorptions from multiple shells in the Homunculus, centered on -500 km s⁻¹, and the Little Homunculus, centered on -150 km s⁻¹, are readily apparent in the high-ionization state ($\phi = 10.404$) but weaken and narrow by three cycles later ($\phi = 13.641$). Multiple spectro-images recorded across cycle 10 at these same PAs showed few changes in structure across the long high-ionization state. While both observations were accomplished at the same PA of 332°, the ensuing 18 years between exposures led to a sixfold increase in stellar flux that further contributed an artificial flux from charge transfer effects in the extended region below $-0''.7$ at $\phi = 13.641$ for (b) and (d).

The fluxes from the spectro-images in Figure 3 are displayed with a matched log(flux) scale to emphasize the changes in absorption. However the nebular continuum, which apparently scatters from dust on the far side of η Car, is very bright across the central arcsecond, then drops by an order of magnitude beyond this region. The edge of the foreground Homunculus lobe ends approximately $1''$ NNW of η Car. The polar cap is about $4''$ SE of η Car, while the aperture is oriented from NNW to SSE.

Most resonant absorption lines include a component from a thermally cold, foreground cloud near 0 km s⁻¹, which is marked by the vertical dashed lines in Figure 3. An additional absorption velocity, $+87$ km s⁻¹, also is present as identified by Walborn et al. (2002) in the Carina Nebula and more recently in Na D $\lambda 5898$ by Pickett et al. (2022).

A broad absorption feature extends from ≈ -550 km s⁻¹ at the bottom of each spectro-image (SSE toward the cap of the Homunculus foreground lobe), shifts to -500 km s⁻¹ at the

Table 2
Identified Lines of Interest

Figure 3 and 4 lines			
Ion	Wavelength	Energy Levels	Lower Energy
Mn II	2576.88	$4s\ a^7S_3-4p\ z^7P_4$	0 eV
Fe II	2756.55	$4s\ a^4D_{7/2}-4p\ z^4F_{9/2}$	1.0 eV
Figure 5 line			
Ion	Wavelength	Energy Levels	Lower Energy
Fe II	2728.35	$4s\ a^4D_{5/2}-4p\ z^4D_{3/2}$	1.0 eV
Figure 6 lines			
Ion	Wavelength	Energy Levels	Lower Energy
Mg I	2852.96	$3s^2\ ^1S_0-3s3p\ ^1P_1$	0.0 eV
Fe II	2756.55	$4s\ a^4D_{7/2}-4p\ z^4F_{9/2}$	1.0 eV
Cr II	2844.08	$4s\ a^6D_{7/2}-4p\ z^6F_{9/2}$	1.5 eV
Figure 9 lines			
Ion	Wavelength	Energy Levels	Lower Energy
Si II	1309.276	$3s^23p\ ^2P_{3/2}-3s3p^2\ ^2S_{1/2}$	0.04 eV
C IV	1550.772	$2\ s^2S_{1/2}-2p\ ^2S_{1/2}$	0 eV

Note. Strong absorption lines of interest.

position of η Car, broadens while shifting to much lower velocities toward the apparent edge of the foreground lobe ($\approx 1''$ NNW of η Car), then loops toward $0\ \text{km s}^{-1}$. A second, broad absorption component begins at the bottom of the spectro-images near $-160\ \text{km s}^{-1}$, shifts slightly to $-150\ \text{km s}^{-1}$ at the position of η Car, then shifts toward $0\ \text{km s}^{-1}$ at the edge of the foreground lobe. The strengths of the broad Homunculus $-500\ \text{km s}^{-1}$ and the Little Homunculus $-150\ \text{km s}^{-1}$ absorptions increase from the high-ionization state, $\phi = 10.404$ (Figure 3(a)), to the low-ionization state, $\phi = 11.037$ (Figure 3(b)). Changes in the absorptions originating from levels near 1 eV are represented by the Fe II $\lambda 2757$ velocity profiles (Figures 3(c) and (d)).

Gull et al. (2006) measured the kinetic temperatures of the $-512\ \text{km s}^{-1}$ component of the Homunculus (760 K) and the $-146\ \text{km s}^{-1}$ component of the Little Homunculus (6370 K) during the cycle 10 high-ionization state. In response to the drop in FUV radiation across the periastron event, the Little Homunculus kinetic temperature dropped to 5000 K. The kinetic temperature of the Homunculus did not change, but most of the H_2 absorptions, driven by FUV excitation, disappeared across the low-ionization state. Note that the lower-velocity absorptions have higher kinetic temperatures (Little Homunculus) than the high higher-velocity absorptions (Homunculus), which are consistent with the faster moving shells being more distant from η Car.

The Homunculus absorption profiles for Fe II $\lambda 2757$ (Figures 3(c) and (d)) are similar to that of Mn II $\lambda 2577$ (Figures 3(a) and (b)) but shallower for both the high- and low-ionization states. Much more substructure within the individual shells (so called, as the structures, somewhat clumpy in nature, appear to define individual surfaces, each with a characteristic velocity within the Homunculus) is noticeable, suggesting that each shell is affected by small variations in velocity,

clumpiness, and excitation. The low-ionization state, $\phi = 11.037$ (Figure 3(d)), shows changes in structure, with notably stronger absorptions shifted to the red relative to the -200 to $-500\ \text{km s}^{-1}$ absorption just NNW of η Car. The changes in structure appear to be continuous, not abrupt, across the position of η Car, indicating extended structures, most likely shells, not individual clumps.

Changing absorption profiles for additional resonant and near-resonant absorption lines are shown in the Appendix.

4.2. Absorption Changes Across the Long Term

The nebular absorptions decreased greatly between the high-ionization states of cycles 10 and 13 in response to the large increase of FUV radiation (Figure 4). In the spectrum of η Car, the broad absorptions centered on $-500\ \text{km s}^{-1}$ (Homunculus) narrowed to an apparently single absorption near $-500\ \text{km s}^{-1}$ while the weaker absorption centered on $-150\ \text{km s}^{-1}$ (Little Homunculus) nearly disappeared. The large decrease in absorption extended to the SSE (toward higher latitudes of the foreground Homunculus lobe), but remained broadened, though weaker beginning about $0''.3$ NNW of η Car. The transition from narrow to broad absorption occurred beginning close to the projected position of η Car then shifting toward lower velocities. Relating to the foreground lobe of the Homunculus, the absorptions dropped toward the cap while lesser changes occurred toward the projected edge of the lobe, about $1''$ to the NNW.

The measured stellar FUV radiation impinging on these structures increased nearly tenfold between 2000 and 2018, which led to increased ionization (Gull et al. 2021), while the measured stellar NUV radiation increased about sixfold. In contrast, the nebular NUV continuum changed marginally, which is consistent with the radiation increase being due to dissipation of the occulter in the LOS, not intrinsic brightening of η Car. Singly ionized metals dominated during the high-ionization state of cycle 10, but the increased FUV (and EUV) led to most metals becoming multiply ionized in the high-ionization state of cycle 13. As a consequence, metal absorptions from these shells disappeared.

Signatures of resonant and near-resonant transitions of multiply ionized metals are deep in the UV, typically below $\text{Ly}\alpha$. Hence signatures of shells with metals in higher ionization states became increasingly inaccessible in the HST/STIS NUV and FUV spectral ranges. The complex, multiple shells in the LOS from the Homunculus and the Little Homunculus virtually disappeared by $\phi = 13.641$, were nearly absent at the position of η Car, but appeared to be less affected in the lobe walls.

The noticeably smaller change in absorptions to the NNW is not surprising given that the walls of the foreground lobe appear to be optically thicker. In part this is because the walls curve toward the edge of the foreground lobe. Additionally, the butterfly boundary, a structure in the disk region located close to η Car, extends from the NW across the projected position of η Car (Chesneau et al. 2005).

These longslit CCD spectra confirm that the decrease in absorption extends over significant angular and spatial distances across the foreground lobe of the Homunculus but do not provide information on how much more of the foreground lobe is affected. Nor do these spectro-images provide information about changes in the back lobes or the skirt region. Infrared and radio observations will be necessary to

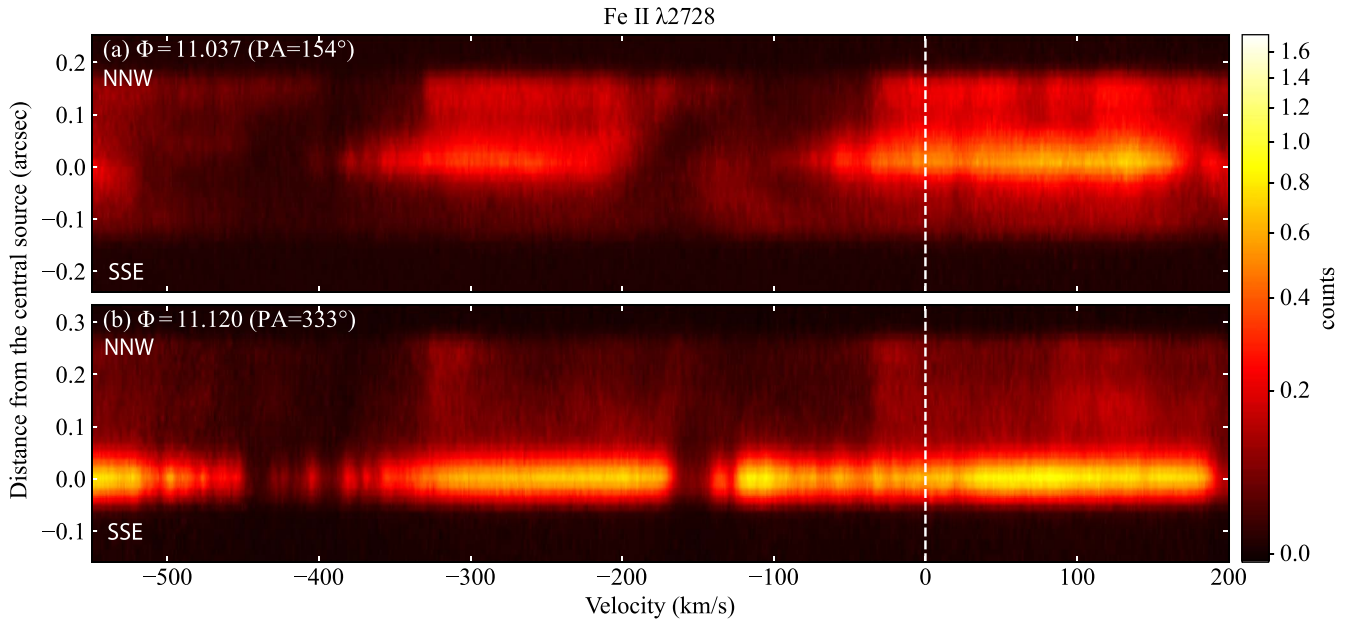


Figure 5. Phase-dependent changes from the low- to high-ionization states recorded in echelle spectro-images of Fe II $\lambda 2728$ absorption structures. Top: η Car was centered in the $0''.3 \times 0''.2$ aperture deep in the low-ionization state ($\phi = 11.037$). Broad, high-velocity absorption from the interacting winds shifts from ≈ -450 km s $^{-1}$ SSE ($-0''.15$) to -550 km s $^{-1}$ centered upon η Car and back to -450 km s $^{-1}$ NNW ($+0''.15$), indicating that the Fe $^{+}$ wind structure is resolved and extends at least a few hundred astronomical units beyond the continuum core. A narrow absorption, centered at -146 km s $^{-1}$ on the star broadens in the NNW as a continuous, shallow absorption extending to -35 km s $^{-1}$ terminated by an emission feature originating from Weigelt B. Bottom: a spectro-image recorded at $\phi = 11.119$, when η Car had returned to the high-ionization state. η Car was positioned at the edge of the aperture in an effort to map structures of Weigelt B and D and the intervening winds. The broad, shallow absorption extends NNW in front of Weigelt D.

determine if additional regions of the Homunculus and interior structures are changing with time.

Changes of absorption across the long term for additional resonant and near-resonant lines are shown in the [Appendix](#).

4.3. Zooming in with STIS Echelle Spectro-images

HST/STIS achieves its best angular resolution in the NUV, with FWHM = $0''.075$, measured directly from the echelle spectro-images presented in Figure 5. The $0''.3 \times 0''.2$ aperture, in combination with the E230H grating formats, resolves a portion of the wind and nebular components at a spectral resolving power of $R=110,000$ for the stellar spectrum. The nebular structure fills the full $0''.2$ width of the $0''.3 \times 0''.2$ aperture, and this leads to a lower nebular resolving power of $R \approx 35,000$. Hence, the various absorption components are less resolved in the nebular portions of the spectro-image than in the stellar spectrum.

Despite the relatively small aperture, the spectro-image fits well within the spacing of NUV echelle orders in the format of the NUV MAMA, allowing for proper detector background measures. This aperture provides some spatial information on changes in velocity structure close to the central star at high spectral resolving power.

Multiple narrow absorption lines are seen in the NUV echelle spectro-images of η Car. Figure 5 displays the spatially and spectrally resolved velocity profiles of Fe II $\lambda 2728$ from two echelle spectro-images, one recorded during the low-ionization state and the other during the early high-ionization state of cycle 11. Superimposed upon the broad wind-absorption components are many narrow components, originating from the multiple velocity-differentiated shells in the LOS previously cataloged by Gull et al. (2006). The broad absorptions, associated with colliding wind structures, extend

beyond the continuum core of η Car ($\approx 0''.075$), the apparent size of which is limited by the angular resolution of HST, most likely which is not the actual size of the continuum core in the NUV.¹⁷

The spectro-image, displayed in Figure 5 (top), was recorded deep in the low-ionization state, $\phi = 11.037$, within a day of the lower-resolution spectro-images displayed in Figures 3(b) and (d). The broad absorptions, associated with the interacting winds, resolved from the continuum core of η Car, extend at least $0''.15$ beyond on both sides, shifting from approximately -450 km s $^{-1}$ from the SSE to -550 km s $^{-1}$ on the star back to -450 km s $^{-1}$ to the NNW. Multiple narrow absorption features are superimposed upon the point-like stellar continuum, but, due to the $0''.2$ width of the $0''.3 \times 0''.2$ aperture, are broadened as the nebular continuum fills the aperture height ($0''.2$) limiting the resolving power, R , to 35,000.

The spectro-image, displayed in Figure 5 (bottom), was recorded in the early high-ionization state, $\phi = 11.119$ with η Car placed at the edge of the aperture in order to record the spectrum of Weigelt D located to the NNW of the star. The broad interacting wind absorption is much weaker, permitting improved visibility of the multiple narrow, nebular absorption features in the LOS from η Car.

4.3.1. High-velocity Absorption Seen in the Echelle Spectro-images

Comparisons of the two spectro-images affirm changes of the stellar and nebular spectra between the low- and high-ionization states. The multiple, narrow-velocity shell absorptions, visible in

¹⁷ Weigelt et al. (2021) used the Very Large Telescope Interferometer to resolve the continuum structure in the mid-infrared to have an FWHM = $0''.0028$ and imaged wind structures in the light of H I Br α that extend $\approx 0''.026$ around η Car. CMFGEN models indicate that the NUV continuum structure of η Car-A is likely more extended than in the IR.

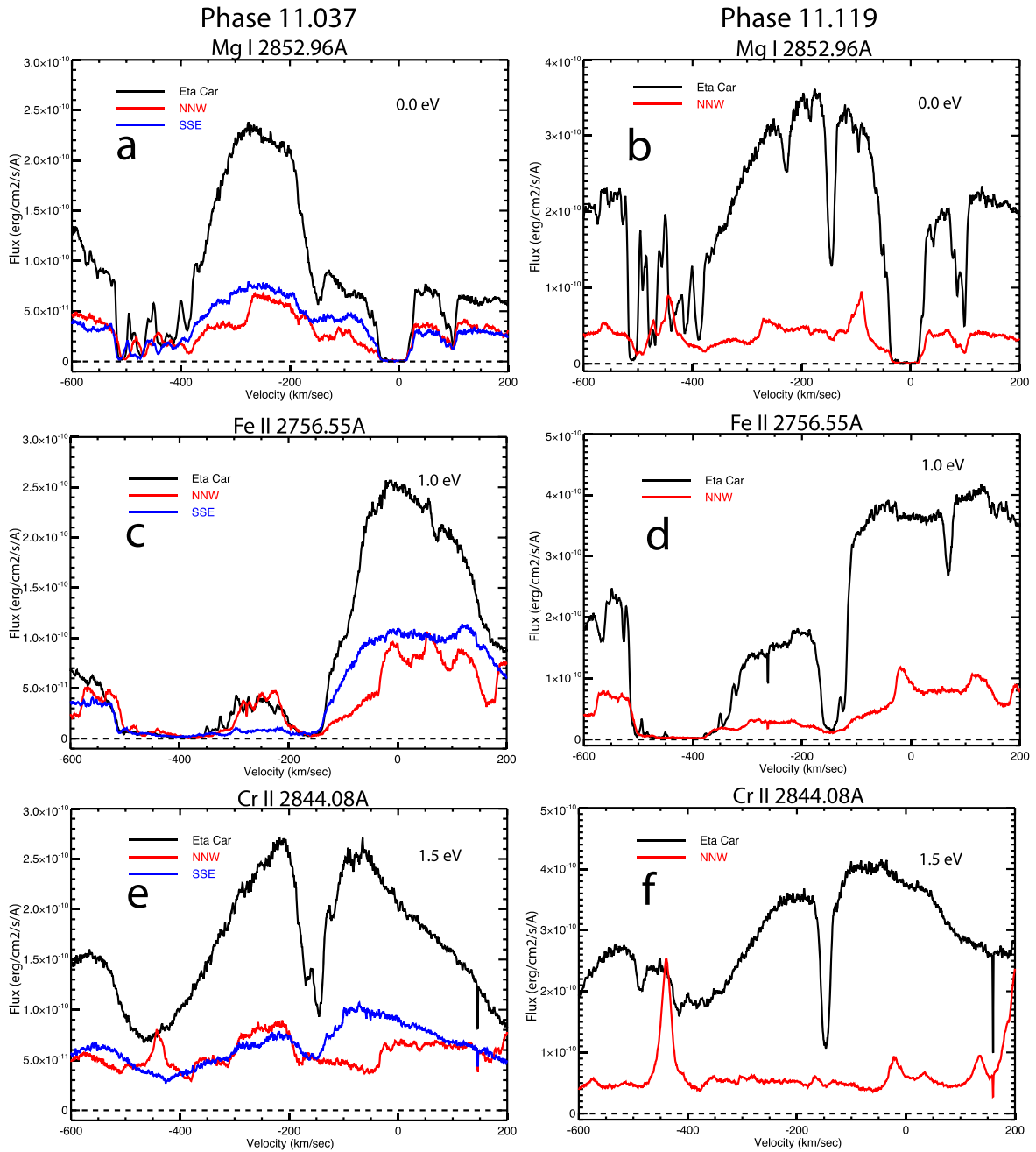


Figure 6. Velocity profiles of three absorption lines that originate from significantly different energy levels during the low-ionization state, $\phi = 11.037$ (left column) and the early high-ionization state, $\phi = 11.119$ (right column). The Mg I $\lambda 2853$ line (0.0 eV; top row) traces changes in multiple shells where neutral gas existed. The Fe II $\lambda 2757$ line (1.0 eV; middle row) is saturated at most shell velocities as singly ionized metals dominate across the multiple shells. The Cr II $\lambda 2844$ line (1.5 eV; bottom row) is dominated by a P Cygni wind profile with strong absorption by shells with velocities between -120 and -190 km s⁻¹, but with only a few high-velocity shells absorbing in the high-ionization state. The velocity profiles are (1) η Car, on the star, (2) NNW, which includes portions of the emission structure, Weigelt D, plus modified scattered starlight to the NNW, and (3) SSE, which is modified scattered starlight. No nebular spectrum SSE of η Car was recorded in the echelle spectro-image recorded at $\phi = 11.119$. Note: the vertical scales on the left and right plots are different—during periastron passage the NUV flux decreases, most likely a consequence of increased line blanketing by the primary wind.

the high-ionization stellar spectrum, are lost in the very strong, broad wind absorption during the low-ionization phase. Both narrow absorption complexes centered on -500 and -150 km s⁻¹ are affected.

More insight on the excitation changes between the high- and low-ionization states comes from examining three absorption line profiles (Figure 6) that rise from different energy levels: Mg I $\lambda 2853$ (0.0 eV), Fe II $\lambda 2757$ (1.0 eV), and Cr II

$\lambda 2844$ (1.5 eV). These velocity profiles were extracted from the same HST/STIS echelle spectra that provided the spectro-images in Figure 5.

The extracted velocity profiles are:

1. The spectrum of η Car extracted with a $0''.075$ wide synthetic aperture for both echelle spectro-images.
2. The nebular spectrum, labeled SSE, was extracted with a $0''.100$ wide synthetic aperture from the echelle spectro-

image recorded at $\phi = 11.037$, offset $0''.100$ SSE from η Car, centered in the $0''.3 \times 0''.2$ aperture. No nebular spectrum to the SSE was recorded at $\phi = 11.119$.

3. The nebular spectrum, labeled NNW was extracted differently from the two spectro-images:
 - (a) For the spectro-image recorded at $\phi = 11.037$, a $0''.100$ wide synthetic aperture, offset $0''.100$ NNW from η Car, centered in the STIS $0''.3 \times 0''.2$ aperture. This enabled measurement of the nebular spectrum both NNW and SSE of η Car at $\phi = 11.037$.
 - (b) For the spectro-image recorded at $\phi = 11.119$, a $0''.150$ wide synthetic aperture offset $0''.200$ NNW as η Car had been placed close to the SSE edge of the STIS $0''.2 \times 0''.3$ aperture.

Velocity profiles are dominated by modified P Cygni wind-line contributions. Groh et al. (2012a), using CMFGEN-based models of the binary winds, estimated the terminal velocity of η Car-A, $V_{\infty A} = -420 \text{ km s}^{-1}$. The wind of η Car-B accelerates the wind-wind collision structures to higher velocities as is noticeable in velocity profile of Cr II $\lambda 2844$ in the low-ionization state (Figure 6(e)) compared to the high-ionization state (Figure 6(f)). The observed V_{∞} shifts from -420 to -550 km s^{-1} (Gull et al. 2022).

The Fe II $\lambda 2757$ line profile (Figures 6(c) and (d)) is saturated across most of the range from -120 to -500 km s^{-1} , but the Mg I $\lambda 2853$ profile in the high-ionization state (Figure 6(b)), allowing for the many narrow velocity components, has a general P Cygni shape. In the low-ionization state (Figure 6(a)), the apparent P Cygni profile appears to exceed -500 km s^{-1} but may be influenced by weaker shells.

Narrow Mg I $\lambda 2853$ absorption structures are readily apparent in the stellar spectrum in both the low- and high-ionization states (Figures 6(a) and (b)). No high-velocity, narrow absorption is obvious in the Cr II $\lambda 2844$ line during the low-ionization state but does appear at -512 and -420 km s^{-1} during the high-ionization state (Figures 6(c) and (d)). These are consistent with the high-velocity shells being partially ionized in both ionization states.

Strong absorption components are present between -100 and -200 km s^{-1} in all three lines, Mg I, Fe II, and Cr II, for both ionization states, indicating that the thermal excitation is significant in shells closer to the FUV source, η Car. Always present is the -146 km s^{-1} component, which is associated with the Little Homunculus. In the high-ionization state, the Fe II $\lambda 2767$ line has a strong absorption at -121 km s^{-1} and is saturated from -140 to -200 km s^{-1} in the low-ionization state. The Cr II $\lambda 2844$ line has a strong -146 km s^{-1} component in the high-ionization state, but adds two components, -121 and -168 km s^{-1} during the low-ionization state.

The nebular continuum in the low-ionization state, extracted $0''.1$ SSE of η Car (labeled SSE in Figure 6), reflects the stellar continuum with saturated absorptions in the Fe II $\lambda 2757$ line from -350 to -500 km s^{-1} and relatively narrow absorptions in Mg I $\lambda 2853$ superimposed upon the P Cygni profile.

In contrast, the nebular continuum in the low-ionization state, extracted NNW of η Car (labeled 'NNW' in Figure 6) contains strong, broad absorptions when compared to the more highly resolved stellar spectrum. Nebular line emission components originate from the background Weigelt D clump, plus broad absorptions extend from -35 to -150 km s^{-1} . The Mg I $\lambda 2853$ line includes a broad absorption extending from

-270 to -370 km s^{-1} , then blends into narrow-line absorptions extending to -510 km s^{-1} . The nebular continuum in the high-ionization state (recorded only to the NNW) again contains very broad absorptions extending from -30 to -150 km s^{-1} .

5. Where is the Occulter/Absorber Located?

In Section 4, we demonstrated that the high-velocity shells extend across significant areas of the Homunculus and Little Homunculus. The FUV absorber must have been much closer to the binary but extended well beyond our LOS. We turn now to examining the spatial structures very close to η Car plus low-velocity absorptions that provide clues to where the absorber appears to be located. In Section 5.1 we examine the spatial extent of recently formed shells seen in forbidden emission. We then demonstrate apparent expansion of the structure which backscatters NUV radiation in our direction (Section 5.2). Low-velocity absorption components seen in atomic species in the FUV and in molecular species in the radio are discussed in Section 5.3. A sketch of the apparent geometry of the absorber relative to the recently formed shells is provided in Section 5.4.

5.1. Recently Formed Compressed Shells by the Interacting Winds

Three emission-line shells were identified in [Fe II] $\lambda 4815$ and [Ni II] $\lambda 7413$ with HST/STIS longslit mappings of the central $2'' \times 2''$ recorded between 2010 and 2012 (Teodoro et al. 2013). Three-dimensional cubes (R.A., decl., and velocity) have been fabricated from spectro-images recorded with the HST/STIS $52 \times 0''.1$ aperture positioned with $0''.05$ spacing. These cubes enabled two-dimensional, isovelocity images in forbidden emission lines. The geometry of these shells formed nested hemispherical structures extending to the SE of η Car. These shells had formed from the dense, slow-moving primary wind compressed by the fast-moving secondary wind across each of three separate periastron passages. Accelerated from 420 to 475 km s^{-1} , the compressed shells persist as their thermal velocities are much less than their expansion velocities. The projected distances, 400 , 900 , and 1400 au , as measured at $\phi = 12.680$, are consistent with their origins occurring during the three periastron passages at the beginnings of cycles 10 through 12.

Gull et al. (2016) extended the mappings in [Fe II] $\lambda 4815$ from $\phi = 12.084$ through 13.113 (2009 to 2015) to track the expansion of these shells across one orbital cycle. Figure 7, a velocity slice from -40 to -80 km s^{-1} , shows the difference in contrast by ratioing shell peaks to shell troughs and thus emphasizes the change in position across one-half binary orbital cycle. This image demonstrates that, across cycle 12, the modulated primary wind extended over the hemispherical volume to the SE, but not to the NW. The faster, less-dense secondary wind, over each lengthy, high-ionization state when η Car-B was beyond the extended wind of η Car-A, evacuates the NW region with the remaining gas being highly ionized by the FUV radiation from η Car-B. The slower, more massive primary wind had been organized into shells moving to the SE by the secondary wind during each of the three previous periastron passages.

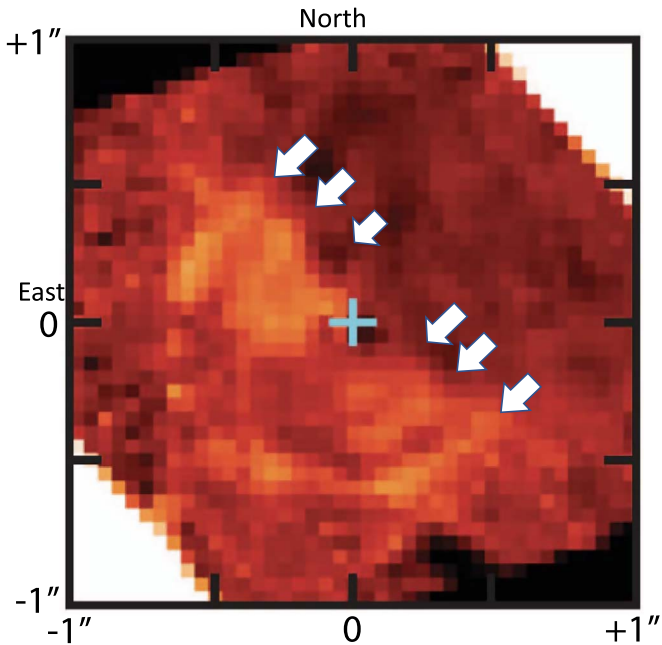


Figure 7. [Fe II] shell expansion. The displayed image is the ratio of the [Fe II] $\lambda 4815$ line recorded at $\phi = 12.516$ and 13.004 to enhance the expanding shells caused by the passage of η Car-B through the extended continuous wind of η Car-A. The velocity range is 40 km s^{-1} centered on -60 km s^{-1} . The three pairs of arrows point to the ends of the three shells found to be expanding outward. These shells do not exist to the NW as the secondary wind has continuously blocked the primary wind throughout the high-ionization state and the FUV radiation from η Car-B has ionized iron to higher ionization states (see Figure 6 in Gull et al. 2016 for additional velocity frames). The + symbol indicates the position of η Car.

5.2. The Expanding Dust Structure Behind the Binary

A noticeable $1''$ diameter structure, illuminated by scattered starlight, is centered on η Car (Figures 3 and 4). The background scattered starlight drops off at greater distances, but still records absorption from extended structures within the Homunculus and Little Homunculus. The spatially limited echelle spectro-images, with higher spatial and spectral resolutions (Figure 5), recorded variations of the extended wind of η Car-A. Such is possible only if the scattered starlight originates from dust that lies beyond η Car and is back, not forward, scattered. The dusty structure that scatters the starlight lies beyond η Car and likely is very-slow-moving ejecta originating with one or both of the historical events.

This scatterer appears to be expanding, most notably to the SSE. A well-defined ridge of scattered starlight, located $0''.5$ SSE of η Car in Figure 4, shifted outward between 2000 ($\phi = 10.404$) and 2018 ($\phi = 13.641$), when the spectro-images were recorded. Spatial slices of the spectral images are compared in Figure 8. Measurements of the SSE ridge position, done with four spectro-images extending from 2540 to 2850 Å and 3900 to 3950 Å, showed this ridge shifted outward $0''.063$ over the 18 year interval. The edge of the scattered-light structure to the NNW was also measured, yielding a shift of $0''.047$ over the 18 year interval. Adopting the accepted distance of η Car, 2300 pc, yields expansion velocities of $39 \pm 3 \text{ km s}^{-1}$ to the SSE and $28 \pm 3 \text{ km s}^{-1}$ to the NNW, which are comparable to the radial velocities of the Weigelt clumps (-45 km s^{-1} ; Zethson 2001). Additional structures at $1''$ – $2''$ distance from η Car, associable with the Little

Homunculus, are likewise seen to be moving outward, but are less well defined.

However, charge transfer inefficiency (CTI), caused by accumulating radiation damage to the CCD, artificially impacts the measured nebular expansions. The CTI effect increased over the 18 year interval and the NUV brightness of η Car also increased. The ridge to the SSE is easily identified, as well as fainter structures in the Homunculus and the Little Homunculus that also expanded. The apparent expansion to the NNE of the scatterer is less defined. Hence the apparent expansion to the NNW must be considered an upper limit, not a true measure. Indeed, the [Fe II] shells as shown in Figure 7 strongly suggest that the secondary wind and ionizing flux of η Car-B may limit the expansion of the background dusty structure to the NW.

5.3. Low Velocities Associated with the Absorber

The infrared flux of η Car, summarized by Mehner et al. (2019), has not changed substantially over the past half century, which is consistent with minimal changes of the binary properties over that period. Stable wind properties over the past 50 years should have produced more than the three shells seen in [Fe II] (Teodoro et al. 2013; Gull et al. 2016) located at greater distances, analogous to the multiple, regularly spaced shells recently detected in dust emission and forbidden radiation surround WR140 (Lau et al. 2022). While the ionizing radiation leading to Fe^+ may be depleted, singly ionized iron absorption is traceable within the Little Homunculus and Homunculus, well beyond these shells. Instead, the massive, slow-moving occulter/absorber has been continuously stopping and absorbing previous shells in the form of shocks.

Based upon the expansion velocity of the three shells, the extended structures associated with the occulter could be located just beyond the outermost shell seen by Teodoro et al. (2013), i.e., just beyond the 1400 au radial distance from η Car. We therefore searched for velocity signatures in the spectra of η Car that are consistent with a structure ejected in the 1840s or 1890s that exceeds that distance.

The occulter in front of the binary could be a clump of similar nature as Weigelt clumps B, C, and D (Weigelt & Ebersberger 1986), additional clumps seen in the IR Butterfly nebula (Chesneau et al. 2005), and likewise clumps seen in [Fe II] (Gull et al. 2016). Adaptive optics imaging in [Fe II] $1.644 \mu\text{m}$ of multiple structures within projected distances of 4000 au from η Car provided epochal origins that ranged from the early 1830s to the late 1910s, being consistent with the Great and Lesser Eruptions (Artigau et al. 2011). While current telescopes and instrumentation are unable to separate extended structure in front of the much brighter η Car, most likely the occulting structure was ejected in this interval.

Such an occulter scenario seems likely because Zethson (2001) measured the radial velocities of Weigelt B and D to be $-45 \pm 4 \text{ km s}^{-1}$. Similar low radial velocities have been measured in front of the binary at radio wavelengths and in the UV using HST/STIS echelle spectra, as discussed in the next two paragraphs.

Chesneau et al. (2005) obtained NIR imagery of η Car and structures within the central region with $0''.1$ angular resolution that showed structure around η Car extending about $0''.5$ to the NW across the position of η Car and about $0''.2$ to the SE (see their Figure 5). Weigelt clumps C and D, located $0''.1$ to $0''.3$ to the NW, are directly ionized by the FUV radiation of η Car.

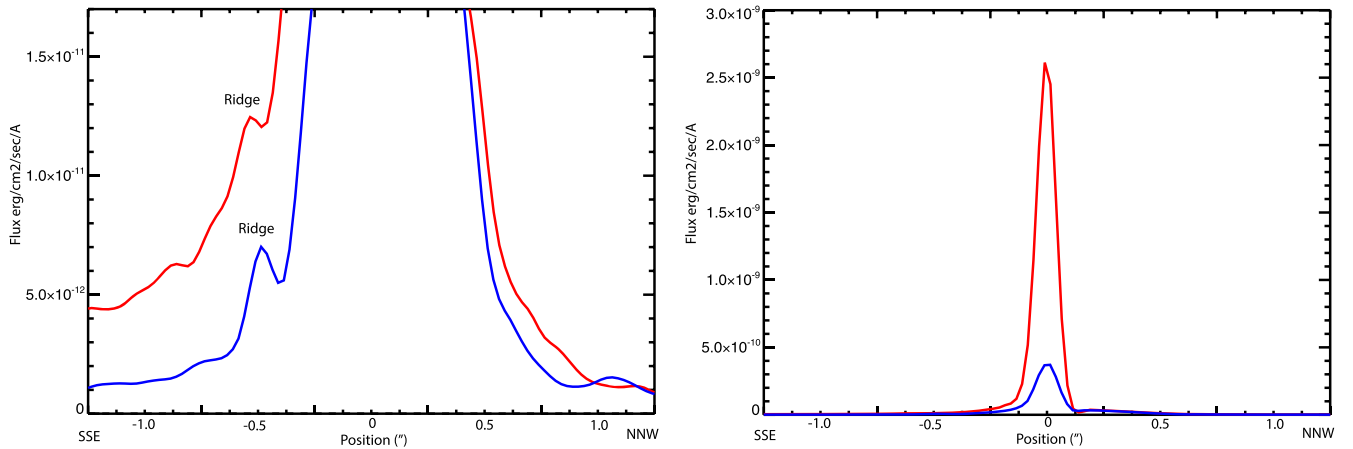


Figure 8. Comparison of the spatial profiles for the spectro-images recorded at $\phi = 10.404$ and $\phi = 13.641$ (see Figure 4). Left: cross section showing the shifts of the SSE ridge at $-0''.5$ and the NNW edge at $+0''.5$. Expansion is notable from the ridge and valley to the SSE and possibly the edge to the NNW. Right: η Car profiles. While the stellar flux in the NUV increased sixfold between 2000 and 2018, the measured FWHM was $0''.11$ for both stellar profiles. Note that both plots are in flux units, not normalized.

They appear to be surface blisters of the dusty, extended structure mapped by Chesneau et al. (2005) as noted by Teodoro et al. (2020).

Bordiu & Rizzo (2019) mapped the central region at 345.8 GHz with the Atacama Large Millimeter/submillimeter Array with $0''.2$ angular resolution, which confirmed continuum emission extending from η Car to the NW (see their Figure 2). They detected line absorption in HCN and H^{13}CN against the continuum from η Car at $V_{\text{lsr}} = -60 \text{ km s}^{-1}$ ($V_{\text{helio}} = -49 \text{ km s}^{-1}$).

The central $2'' \times 2''$ region was mapped in [Fe II] $\lambda 4816$ with $R = \lambda/\delta\lambda = 10,000$ and $0''.1$ angular resolution (Gull et al. 2016). Their Figure 3, which shows changes across one binary orbital cycle, shows a bright emission structure to the NW that includes Weigelt C and D. Reexamination of these data demonstrated that this narrow-line emission structure extends to within $0''.1$ (~ 230 au) of η Car, but is not present to the SE. The slowly varying central velocity terminates close to η Car at $-49 \pm 4 \text{ km s}^{-1}$, the velocity of the molecular absorptions published by Bordiu & Rizzo (2019). Weigelt & Kraus (2012) found the origin of the Weigelt clumps to be consistent with the 1890s event.

Smith (2004) measured the systemic velocity of the Homunculus to be $V_{\text{helio}} = -8.1 \pm 1 \text{ km s}^{-1}$. Nielsen et al. (2007) adopted that velocity for the binary system velocity, finding consistency while deriving the binary orbital parameters. If we assume this to be the central velocity of the binary, the expansion velocity, -41 km s^{-1} , originating from the 1890s event with no intervening material, translates to 1000 au. For comparison, Teodoro et al. (2013) found the outermost shells to be $0''.8$ (1850 au) distant from η Car, but also noted that the shells appeared to be moderately accelerated. The systemic velocity of the binary could be slightly different. We do not know if the bipolar ejection of the Homunculus was symmetric for both lobes. The expansion velocity of the occulter could be significantly (smaller) larger in the LOS. If the systemic velocity of the binary differed by 10 km s^{-1} , the distance estimate would (decrease) increase to 1250 au (750 au).

Additional searches were done for similar absorption velocities in the HST/STIS UV echelle spectra recorded in both the high- and low-ionization states (Table 1). Two low-velocity absorption profiles were measured in Si II $\lambda 1309$ and C IV $\lambda 1551$ (Figure 9). The two strongest absorptions in Si II,

-32 and -18 km s^{-1} , presumably are from slower, singly ionized structures, which is to be expected as many weaker analogs of the Weigelt clumps were found at similar velocities in the central $1''$ diameter region in [Fe II] $\lambda 4815$ (Gull et al. 2016). A relatively weak absorption is present at -50 km s^{-1} .

A very strong velocity component is present in C IV $\lambda 1551$ centered at -40 km s^{-1} , extending from -100 to $+20 \text{ km s}^{-1}$. (Note that this C IV resonant line is the red member of the well-known doublet. Absorption at this velocity from the shorter wavelength member, 1548 \AA , is masked by the strong, wind-wind, blueshifted component of 1551 \AA .) Both Si IV $\lambda \lambda 1304, 1403$ velocity profiles (not shown) are completely saturated between -60 and -20 km s^{-1} , which reinforces the presence of the -50 km s^{-1} gas somewhere in the LOS. The strengths of these absorption profiles changed little from high-ionization to low-ionization states across both periastron passages, 10/11 and 13/14, despite the considerable change in FUV flux. The strong C IV $\lambda 1549$ is suggestive of a shock, which could be evidence of ongoing shell collisions with the occulting structure. This low-velocity profile of C IV persisted across all FUV spectra recorded by the STIS across cycles 10/11 and 13/14.

If mappings continued across cycles 13 and 14, we suggest that the outermost shell would have continuously disappeared, having collided with the occulter/absorber with a new shell forming close to η Car. However, with the disappearance of the occulter, would that be evidence that the absorber has completely dissipated? Only follow-up observations would tell. High-spatial-resolution studies of molecular and ionic species in radio spectra may provide additional insight along with future UV/visible studies.

We conclude that the occulter is 1000 au from η Car with a lower limit of 500–2000 au.

5.4. The Geometry of the Absorber

A schematic of the extended occulter structures close to η Car is presented in Figure 10. The three recently formed shells, as mapped in 2012, lie closest to η Car with the occulter just external to the outermost shell. Under the scenario presented above, by 2022, two more shells would have formed while the two outermost shells have been destroyed by collision with, and absorption by, the occulter. At any given

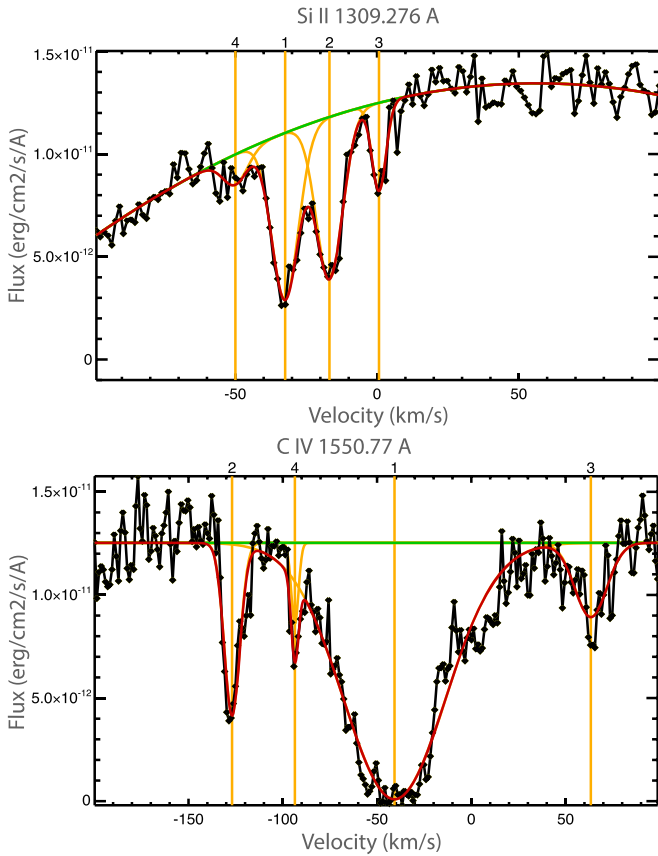


Figure 9. Low-velocity absorptions attributable to the occulter. Top: Si II $\lambda 1309$ velocity profile. Two strong absorptions centered at -18 and -32 km s^{-1} with two weaker components at -50 and $+1$ km s^{-1} (foreground cloud). Bottom: C IV $\lambda 1551$ velocity profile with a strong absorption centered at -39 km s^{-1} and extending from -20 to -70 km s^{-1} . Observation recorded at $\phi = 13.886$.

time three shells fill a volume to the SE somewhat larger than a hemisphere based upon the expansion imagery noted by Gull et al. (2016) and the remaining hemisphere to the NW with high ionization by the FUV flux from η Car-B.

The occulter partially obscures our LOS from η Car. Hillier et al. (2006) noted that the equivalent width of $H\alpha$ in the direct stellar spectrum, recorded in the early 2000s, was twice that predicted by CMFGEN models (Hillier et al. 2006). They explained that the absorber occulted the central core (where the continuum originates) more than it did of the primary wind. Indeed over the past two decades, the equivalent width of $H\alpha$ has decreased, trending toward the value seen in scattered starlight from portions of the Homunculus (Damineli et al. 2021). Direct imagery with the HST/Faint Object Camera (FOC) in the UV (Weigelt et al. 1995) previously showed the nebulosity surrounding η Car to be clumpy in nature and also demonstrated the high relative brightness of the three ejected clumps. This additionally suggests the existence of an extended, nonuniform occulter.

The dusty structure that backscatters light from η Car is sketched beyond η Car. The periastron passage is in this general direction and suggests that a large amount of material may have been ejected during one or both of the two eruptions. Perhaps radio observations of molecular emissions may provide additional information on this structure. The broad absorption features to the NNW in Figures 3 through 4 are suggestive of interaction of the winds with this structure.

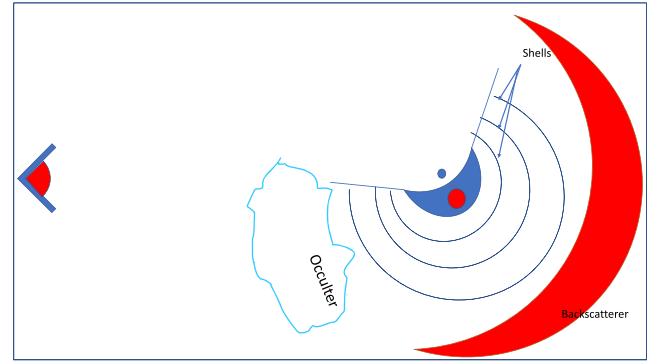


Figure 10. Sketch of the structures in close proximity to the binary (not to scale). The massive primary, η Car-A, has a very extended wind structure (dark blue) which is modified by the lesser, but faster, wind of η Car-B. Three shells of compressed primary wind, seen in [Fe II] $\lambda 4815$ (Teodoro et al. 2013), are located beyond the current wind structure of the binary. The occulter has a structure that extends to one side of the binary. The occulter blocked one side of the extended primary wind and strongly blocked the central core, but as the occulter dissipated, our LOS to the core has become increasingly transparent. The leading edge is toward the observer with rotation counterclockwise. On the far side of η Car a dusty structure scatters light from the binary back toward the observer.

5.5. Origin of the Occulting Structure

The velocity of C IV, -40 km s^{-1} , is close to the velocity measured in HCN and $H^{13}\text{CN}$, -49 km s^{-1} , which suggests a related origin, namely the occulting structure. Moreover, these velocities are close to the velocities measured of Weigelt BD, -45 km s^{-1} , by Zethson (2001). Weigelt & Kraus (2012) found the proper motion of Weigelt D corresponded to an origin of 1880 ± 20 yr, which is consistent with an origin from the Lesser Eruption of the 1890s.

The occulting structure must be well within both the Homunculus and the Little Homunculus as both structures responded to the long-term changes, as demonstrated in Figure 4. Moreover the much-slower-moving, occulting structure, were it ejected in the Great Eruption, would likely have blocked the multiple shells with velocities exceeding its 50 km s^{-1} velocity. Indeed the occulting structure has protected the multiple shells from the apparently ongoing, interacting winds found to be expanding at 470 km s^{-1} (Teodoro et al. 2016). Only three recently formed shells were seen in [Fe II] and [Ni II]. Earlier shells appear to have been blocked and absorbed by the occulting structure.

An alternative explanation might be that the occulter was moving tangentially as a knife edge blocking η Car across the past half century. However it appears unlikely that such a structure would uncover η Car and the very extended region as seen in Figure 4 within the observed 18 yr interval. Occam's razor leads to the simplest explanation, namely a dissipating occulting structure.

6. Conclusions

The brightening of η Car over the past two decades has been attributed to changing properties of the interacting winds. Davidson et al. (2018) claimed that the mass-loss rate of the primary is decreasing. This contradicts the repeatability of the increase in the depth of the P Cygni absorption (Damineli et al. 2022). Espinoza Galeas (2021) pointed out that the X-ray flux measures at apastron have not changed appreciably nor has the X-ray light curve changed noticeably in the multiple periastron passage approaches that have been closely monitored.

Recovery of the postperiastron flux toward the high-ionization state does vary from passage to passage and is thought to be governed by details of the reforming bowshock structure as it is rebuilt from the clumpy luminous blue variable (primary) wind (Davies et al. 2008). This suggests further investigation.

Figures 3, 4, A1, and A2 demonstrate that a large portion of both the Homunculus and especially the Little Homunculus foreground lobes became more highly ionized between $\phi = 10.602$ and 13.641. Indeed the velocity signatures of singly ionized iron, which traced the structure of the Little Homunculus at $\phi = 10.404$, completely disappeared by $\phi = 13.641$ and the broad absorptions tracing the Homunculus extending from SSE of η Car to the position of η Car narrowed to the -512 km s^{-1} component. The singly ionized metal lines are still present to a lesser degree in the nebular spectra west of η Car at $\phi = 13.641$ and extend well beyond Weigelt clump D. The decline in extinction by the occulter produced a tenfold increase in FUV flux and higher nebular ionization with the destruction of H_2 at -512 km s^{-1} in the intervening years from 2004 to 2018.

This study demonstrates that the multiple shells within the Homunculus and Little Homunculus have changed in ionization state over the past two decades. This is a direct result of the tenfold increase in FUV radiation noted by Gull et al. (2021, 2022). The studies by Damineli et al. (2021) and those summarized therein show that the flux increase is caused by a dissipating occulter, first suggested by Hillier & Allen (1992).

The long-term increase in the LOS P Cygni absorptions may seem contradictory to the disappearance of nebular absorption in the UV. However, the strengths of the P Cygni absorptions in the nebular-scattered starlight were much stronger three decades ago. The explanation remains that dust in our LOS was blocking the continuum-emitting core more so than the much-more-extended primary wind, which is the source of the P Cygni profile. As noted by Mehner et al. (2019), all evidence points to a stable flux from the massive binary over the past half century. The apparent increase in FUV flux, due to the dissipating extinction in our LOS, led to the tenfold increase in the FUV and resulted in higher ionization of nebular shells in the foreground Homunculus lobe and the destruction of H_2 .

The combination of HST/STIS spectro-imagery with published studies in the visible (Weigelt & Ebersberger 1986), in the infrared (Chesneau et al. 2005), and the radio (Bordiu & Rizzo 2019) leads to a picture that the occulter in front of the binary is an extended clump of similar nature to Weigelt clumps B, C, and D and fainter clumps seen in the infrared Butterfly nebula.

Destruction of the intervening dust from the occulter in the long term has increased the ionization of multiple shells within the Homunculus from neutral and singly ionized metals to multiply ionized metals. Resonant lines for multiply ionized metals are in the EUV. More FUV radiation now reaches throughout the Homunculus. Eventually, as the Homunculus continues to expand, most dust within the Homunculus is likely to be modified and/or destroyed. With dust destruction, the scattered light that currently traces the spatial structure of the Homunculus will gradually disappear. As the ejecta become increasingly diluted, will mix with the interstellar medium (ISM), currently at much larger distances due to previous winds from η Car driving out the ISM.

The Homunculus, when the dust is destroyed and the associated gases multiply ionized along with continued shell

expansion, will become nearly transparent as likely has happened with ejecta from the winds of other massive binaries. η Car and its ejecta, already known as an astrophysical laboratory, as future observations are made, will continue to provide insight into the evolution of ejecta from massive stars.

This study, limited to line absorptions against η Car and nebular-scattered starlight, has focused on changes in the LOS from η Car and a relatively small area surrounding η Car. Changes are obviously occurring throughout the Homunculus as the UV radiation eats away at the dust and molecules along with the ongoing expansion.

Future studies, especially in the FUV, become all the more important. Hopefully the HST/STIS access will continue through the next decade as monitoring of changes across the next periastron in 2025 now becomes key to confirming the changes seen across periastron passage 14. Important studies of the entire Homunculus are now warranted in the IR and radio spectral regions. Specifically, radio studies of atomic and molecular shocks in the close vicinity of η Car should be seriously considered. And along with ongoing studies, modeling of the massive binary system and its wind interactions and its radiation on the expanding ejecta continue to be needed.

Acknowledgments

N.R. acknowledges funding from HST programs 15611 and 15992, which were accepted as supplementary observations associated with CHANDRA programs 20200564 and 21200197. M.F.C. is supported under the CRESST-II cooperative agreement #80GSFC17M0002 with the NASA/Goddard Space Flight Center. A.D. received funding from FAPESP 2011/51680-6 and and CNPq 301490/2019-8. A.F.J.M. is grateful for financial aid from NSERC (Canada).

We thank the referee for insightful comments leading to a clearer presentation.

Facility: HST/STIS.

Appendix Nebular Absorptions in 2560–2610 Å

Figures A1 and A2 demonstrate that the absorption profiles shown in Figure 3 occur repeatedly in multiple metal lines in the NUV, with details influenced by the physical conditions and the transition probabilities of each metal line. In simplest

Table A1
Identified Lines of Interest

Figure A1 lines			
Ion	Wavelength	Energy levels	Lower Energy
Mn II	2576.88	4 s $a^7S_3-4p z^7P_4$	0.0 eV
Fe II	2586.65	4 s $a^6D_{9/2}-4p z^6D_{7/2}$	0.0 eV
Fe II	2600.17	4 s $a^6D_{9/2}-4p z^6D_{9/2}$	0.0 eV
Mn II	2594.50	4 s $a^7S_3-4p z^7P_3$	0.0 eV
Mn II	2606.46	4 s $a^7S_3-4p z^7P_2$	0.0 eV
Figure A2 lines			
Ion	Wavelength	Energy levels	Lower Energy
Fe II	2740.36	4 s $a^4D_{7/2}-4p z^4D_{7/2}$	1.0 eV
Fe II	2747.30	4 s $a^4D_{3/2}-4p z^4F_{5/2}$	1.1 eV
Fe II	2750.13	4 s $a^4D_{5/2}-4p z^4F_{7/2}$	1.1 eV
Fe II	2756.55	4 s $a^4D_{7/2}-4p z^4F_{9/2}$	1.0 eV

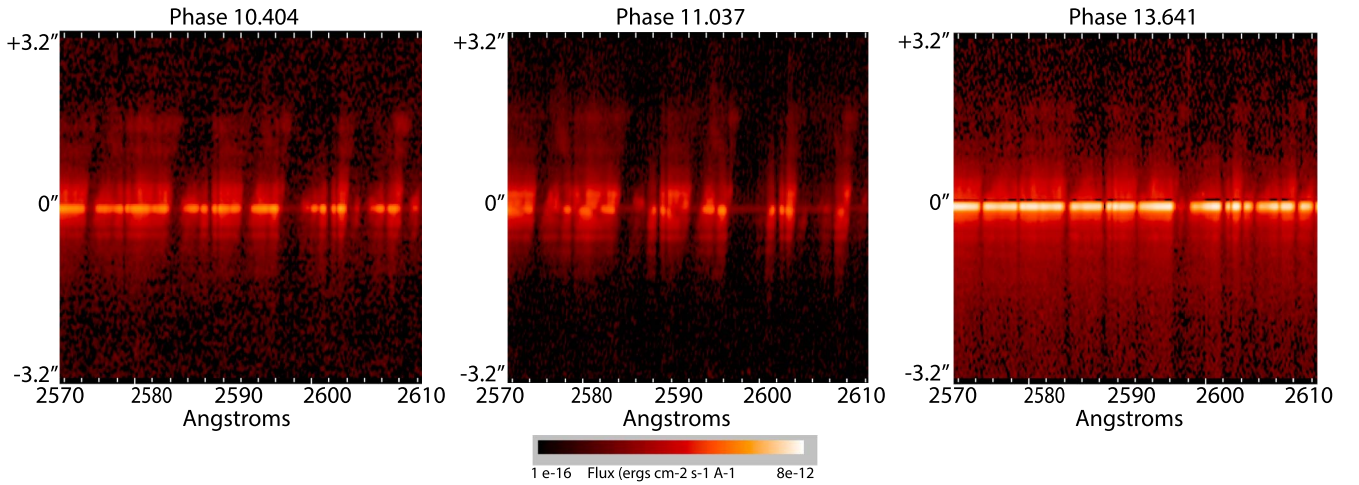


Figure A1. Changes in absorption lines originating from the ground state. Within one orbital cycle strong absorptions in the high-ionization state (left, $\phi = 10.404$) increase to even stronger absorptions in the low-ionization state (middle, $\phi = 11.037$). Two broad velocity complexes centered on -500 and -150 km s^{-1} at the star position extend from ≈ -550 and -200 km s^{-1} SSE (below the position of η Car) to near 0 km s^{-1} to the NNW (above the position of η Car). Three orbital cycles later, the absorptions in the high-ionization state have all but disappeared in the SSE (right, $\phi = 13.641$) caused by the tenfold increase in FUV radiation. Only one component, -513 km s^{-1} associated with the Homunculus, remains SSE (bottom) of η Car, but a broader component extending from the star position remains to the NNW which demonstrates that the absorption remains in the walls at lower elevations of the Homunculus foreground lobe. The 0 km s^{-1} IS absorption lines serve as velocity reference for each of the shell structures. The leftmost absorption line, Mn II $\lambda 2577$, is described in more detail and in velocity space in Figures 3 and 4.

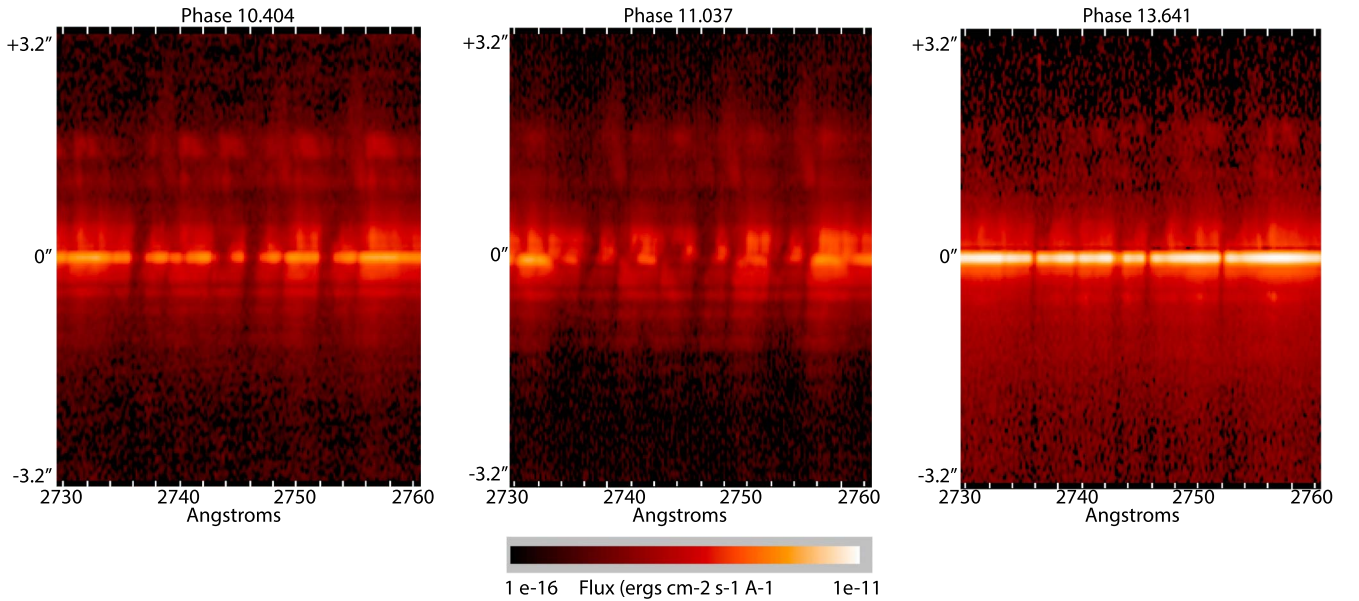


Figure A2. Comparison of changes of Fe II absorption lines originating from the 1.0 eV energy level. As with the ground state absorbers, the absorption increases between the high-ionization state (left, $\phi = 10.404$) and the low-ionization state (middle, $\phi = 11.037$). The absorptions nearly disappear in the SSE (below the position of η Car), other than the -513 km s^{-1} component, in the high-ionization state three orbital cycles later (right, $\phi = 13.641$). Likewise, the broad absorption remains to the NNW (above the position of η Car) at lower latitudes of the foreground lobe. The right-most absorption line, Fe II $\lambda 2757$, is presented in more detail and in velocity space in Figures 3 and 4.










terms, the ionization state of the shells within the Homunculus are strongly influenced by ionizing FUV radiation. The absorptions from singly ionized metals increase across the binary orbit from the high-ionization ($\phi = 10.404$) to low-ionization ($\phi = 11.037$) states. The absorptions in the two high-ionization states ($\phi = 10.404$ and 13.641) should be very similar. However the increased FUV radiation has increased the ionization levels of the shells; the trend of disappearing absorption is general. The strongest lines are listed in Table A1.

The plots are displayed with the y-axes the same in angular interval for direct comparison, but the x-axes span different spectral ranges. Many of the Fe II lines extend beyond the

continuum background, which terminates at about $1''.8$ NNW, changing from absorption to emission, characteristic of the oft-described P Cygni profile, but in this case is caused by the spatially resolved nebular structure.

ORCID iDs

Theodore R. Gull <https://orcid.org/0000-0002-6851-5380>
 Henrik Hartman <https://orcid.org/0000-0001-9853-2555>
 Mairan Teodoro <https://orcid.org/0000-0002-8289-3660>
 D. John Hillier <https://orcid.org/0000-0001-5094-8017>
 Michael F. Corcoran <https://orcid.org/0000-0002-7762-3172>

Augusto Daminieli  <https://orcid.org/0000-0002-7978-2994>
 Kenji Hamaguchi  <https://orcid.org/0000-0001-7515-2779>
 Thomas Madura  <https://orcid.org/0000-0001-7697-2955>
 Anthony F. J. Moffat  <https://orcid.org/0000-0002-4333-9755>
 Patrick Morris  <https://orcid.org/0000-0002-5186-4381>
 Krister Nielsen  <https://orcid.org/0000-0003-2636-7663>
 Noel D. Richardson  <https://orcid.org/0000-0002-2806-9339>
 Ian R. Stevens  <https://orcid.org/0000-0001-7673-4340>
 Gerd Weigelt  <https://orcid.org/0000-0001-9754-2233>

References

- Artigau, É., Martin, J. C., Humphreys, R. M., et al. 2011, *AJ*, **141**, 202
 Bordiu, C., & Rizzo, J. R. 2019, *MNRAS*, **490**, 1570
 Chesneau, O., Min, M., Herbst, T., et al. 2005, *A&A*, **435**, 1043
 Corcoran, M. F. 2005, *AJ*, **129**, 2018
 Corcoran, M. F., Hamaguchi, K., Pittard, J. M., et al. 2010, *ApJ*, **725**, 1528
 Daminieli, A. 1996, *ApJL*, **460**, L49
 Daminieli, A., Conti, P. S., & Lopes, D. F. 1997, *NewA*, **2**, 107
 Daminieli, A., Fernández-Lajús, E., Almeida, L. A., et al. 2019, *MNRAS*, **484**, 1325
 Daminieli, A., Hillier, D. J., Navarete, F., et al. 2022, arXiv:2211.01445
 Daminieli, A., Navarete, F., Hillier, D. J., et al. 2021, *MNRAS*, **505**, 963
 Davidson, K., Ebbets, D., Weigelt, G., et al. 1995, *AJ*, **109**, 1784
 Davidson, K., Ishibashi, K., Martin, J. C., & Humphreys, R. M. 2018, *ApJ*, **858**, 109
 Davies, B., Vink, J., & Oudmaijer, R. 2008, in ASP Conf. Ser. 388, Mass Loss From Stars and The Evolution of Stellar Clusters, ed. A. de Koter, L. J. Smith, & L. B. F. M. Lamers (San Francisco, CA: ASP), 71
 Espinoza Galeas, D. A. 2021, PhD thesis, The Catholic Univ. America
 Gaviola, E. 1950, *ApJ*, **111**, 408
 Groh, J. H., & Daminieli, A. 2004, *IBVS*, **5492**, 1
 Groh, J. H., Hillier, D. J., Madura, T. I., & Weigelt, G. 2012a, *MNRAS*, **423**, 1623
 Groh, J. H., Madura, T. I., Hillier, D. J., Kruij, C. J. H., & Weigelt, G. 2012b, *ApJL*, **759**, L2
 Gull, T. R., Hillier, D. J., Hartman, H., et al. 2022, *ApJ*, **933**, 175
 Gull, T. R., Kober, G. V., & Nielsen, K. E. 2006, *ApJS*, **163**, 173
 Gull, T. R., Madura, T. I., Teodoro, M., et al. 2016, *MNRAS*, **462**, 3196
 Gull, T. R., Morris, P. W., Black, J. H., et al. 2020, *MNRAS*, **499**, 5269
 Gull, T. R., Navarete, F., Corcoran, M. F., et al. 2021, *ApJ*, **923**, 102
 Hillier, D. J., & Allen, D. A. 1992, *A&A*, **262**, 153
 Hillier, D. J., Davidson, K., Ishibashi, K., & Gull, T. 2001, *ApJ*, **553**, 837
 Hillier, D. J., Gull, T., Nielsen, K., et al. 2006, *ApJ*, **642**, 1098
 Ishibashi, K., Corcoran, M. F., Davidson, K., et al. 1999, *ApJ*, **524**, 983
 Ishibashi, K., Gull, T. R., Davidson, K., et al. 2003, *AJ*, **125**, 3222
 Lau, R. M., Hankins, M. J., Han, Y., et al. 2022, *NatAs*, **6**, 1308
 Madura, T. I., Gull, T. R., Okazaki, A. T., et al. 2013, *MNRAS*, **436**, 3820
 Madura, T. I., Gull, T. R., Owocki, S. P., et al. 2012, *MNRAS*, **420**, 2064
 Mehner, A., Davidson, K., Ferland, G. J., & Humphreys, R. M. 2010, *ApJ*, **710**, 729
 Mehner, A., de Wit, W. J., Asmus, D., et al. 2019, *A&A*, **630**, L6
 Morse, J. A., Davidson, K., Bally, J., et al. 1998, *AJ*, **116**, 2443
 Nielsen, K. E., Corcoran, M. F., Gull, T. R., et al. 2007, *ApJ*, **660**, 669
 Pickett, C. S., Richardson, N. D., Gull, T. R., et al. 2022, *ApJ*, **937**, 85
 Pittard, J. M., & Corcoran, M. F. 2002, *A&A*, **383**, 636
 Smith, N. 2004, *MNRAS*, **351**, L15
 Smith, N. 2006, *ApJ*, **644**, 1151
 Smith, N. 2017, *MNRAS*, **471**, 4465
 Smith, N., & Frew, D. J. 2011, *MNRAS*, **415**, 2009
 Strawn, E., Richardson, N. D., Moffat, A. F. J., et al. 2023, *MNRAS*, **519**, 5882
 Teodoro, M., Daminieli, A., Heathcote, B., et al. 2016, *ApJ*, **819**, 131
 Teodoro, M., Gull, T. R., Bautista, M. A., et al. 2020, *MNRAS*, **495**, 2754
 Teodoro, M., Madura, T. I., Gull, T. R., Corcoran, M. F., & Hamaguchi, K. 2013, *ApJL*, **773**, L16
 Thackeray, A. D. 1953, *MNRAS*, **113**, 211
 Verner, E. M., Bruhweiler, F., & Gull, T. R. 2005, *ApJ*, **624**, 973
 Walborn, N. R., Danks, A. C., Vieira, G., & Landsman, W. B. 2002, *ApJS*, **140**, 407
 Weigelt, G., Albrecht, R., Barbieri, C., et al. 1995, *RMxAC*, **2**, 11
 Weigelt, G., & Ebersberger, J. 1986, *A&A*, **163**, L5
 Weigelt, G., Hofmann, K. H., Schertl, D., et al. 2021, *A&A*, **652**, A140
 Weigelt, G., & Kraus, S. 2012, in *Eta Carinae and the Supernova Impostors*, ed. K. Davidson & R. M. Humphreys, Vol. 384 (Boston: Springer), 129
 Zethson, T. 2001, PhD thesis, Lunds Universitet (Sweden)